10-6-2014

A combined method to quantify the retinal metabolic rate of oxygen using photoacoustic ophthalmoscopy and optical coherence tomography

Wei Song
Northwestern University; Harbin Institute of Technology

Qing Wei
Northwestern University

Wenzhong Liu
Northwestern University

Tan Liu
Northwestern University

Ji Yi
Northwestern University

See next page for additional authors

Recommended Citation
Song, W. et al. A combined method to quantify the retinal metabolic rate of oxygen using photoacoustic ophthalmoscopy and optical coherence tomography.Sci. Rep.4, 6525; DOI:10.1038/srep06525 (2014).

Authors
Wei Song, Qing Wei, Wenzhong Liu, Tan Liu, Ji Yi, Nader Sheibani, Amani A. Fawzi, Robert A. Linsenmeier, Shuliang Jiao, and Hao F. Zhang

SCIENTIFIC REPORTS

OPEN

SUBJECT AREAS:
OPTICAL IMAGING
ULTRASOUND

Received
17 March 2014

Accepted
15 September 2014

Published
6 October 2014

Correspondence and requests for materials should be addressed to H.F.Z. (hfzhang@northwestern.edu)

* These authors contributed equally to this work.

A combined method to quantify the retinal metabolic rate of oxygen using photoacoustic ophthalmoscopy and optical coherence tomography

Wei Song[1,6]*, Qing Wei[1]*, Wenzhong Liu[1]*, Tan Liu[1], Ji Yi[1], Nader Sheibani[2], Amani A. Fawzi[3], Robert A. Linsenmeier[1,3,4], Shuliang Jiao[5] & Hao F. Zhang[1,3]

[1]Department of Biomedical Engineering, Northwestern University, Evanston, IL 60208, USA, [2]Department of Ophthalmology and Visual Sciences, University of Wisconsin-Madison, WI 53792, USA, [3]Department of Ophthalmology, Northwestern University, Chicago, IL 60611, USA, [4]Department of Neurobiology and Physiology, Northwestern University, Evanston, IL 60208, USA, [5]Department of Biomedical Engineering, Florida International University, Miami, FL 33174, USA, [6]Department of Physics, Harbin Institute of Technology, 92 West Da-Zhi Street Nangang District, Harbin, Heilongjiang 150080, China.

Quantitatively determining physiological parameters at a microscopic level in the retina furthers the understanding of the molecular pathways of blinding diseases, such as diabetic retinopathy and glaucoma. An essential parameter, which has yet to be quantified noninvasively, is the retinal oxygen metabolic rate ($rMRO_2$). Quantifying $rMRO_2$ is challenging because two parameters, the blood flow rate and hemoglobin oxygen saturation (sO_2), must be measured together. We combined photoacoustic ophthalmoscopy (PAOM) with spectral domain-optical coherence tomography (SD-OCT) to tackle this challenge, in which PAOM measured the sO_2 and SD-OCT mapped the blood flow rate. We tested the integrated system on normal wild-type rats, in which the measured $rMRO_2$ was 297.86 ± 70.23 nl/minute. This quantitative method may shed new light on both fundamental research and clinical care in ophthalmology in the future.

The demand for treating blindness and low vision continue to escalate as human longevity increases worldwide. By 2004[1], for example, blindness and low vision had affected more than three million Americans aged 40 years and older; by 2010[2], 285 million people globally were affected. More than 80% of such visual impairments were caused by eye diseases[1], which include glaucoma, diabetic retinopathy (DR), age-related macular degeneration (AMD), and cataracts[1,2]. Alterations in oxygen metabolism are believed to be involved in most of these diseases[3,4]. For instance, hypoxia in the glaucomatous retina can damage the optic nerve head, partially due to insufficient vascular perfusion[5]. In DR, the loss of pericytes is often associated with poorly regulated blood flow[6], which can further lead to retinal vascular occlusion and retinal hypoxia[7]. In AMD, abnormalities in retinal perfusion have also been reported[8]. Perturbations in retinal oxygenation can prompt, for example, degeneration of retinal neurons, loss of photoreceptors, and onset of neovascularization, eventually causing visual impairment. Therefore, the precise measurement of retinal oxygen metabolic rate ($rMRO_2$) can be critical in investigating these blinding diseases.

Non-invasive $rMRO_2$ quantification has been proposed for decades[9,10] without being successfully demonstrated. Obtaining $rMRO_2$ measurements is challenging because it requires measuring retinal blood flow and oxygen saturation (sO_2) together. Advances in Doppler spectral domain optical coherence tomography (SD-OCT) makes it possible to precisely detect retinal blood flow[11]. The main obstacle is accurately measuring retinal sO_2. To measure retinal sO_2, researchers have used oxygen-sensitive electrodes and magnetic resonance imaging[12–15], but these efforts are usually restricted to terminal experiments and/or limited by low spatial resolution.

To resolve retinal sO_2 noninvasively and with a high spatial resolution, researchers have mainly focused on multi-spectral fundus photography based oximetry[16]. Owing to the distinct light absorption spectrum between oxygenated and deoxygenated hemoglobins[16,17], multi-wavelength fundus photography can assess the sO_2 in retinal vessels. Specifically, optical density of a retinal blood vessel, which is the logarithm of the ratio between detected backscattered light intensities from the vessel and its adjacent retinal tissues[16], is obtained at several

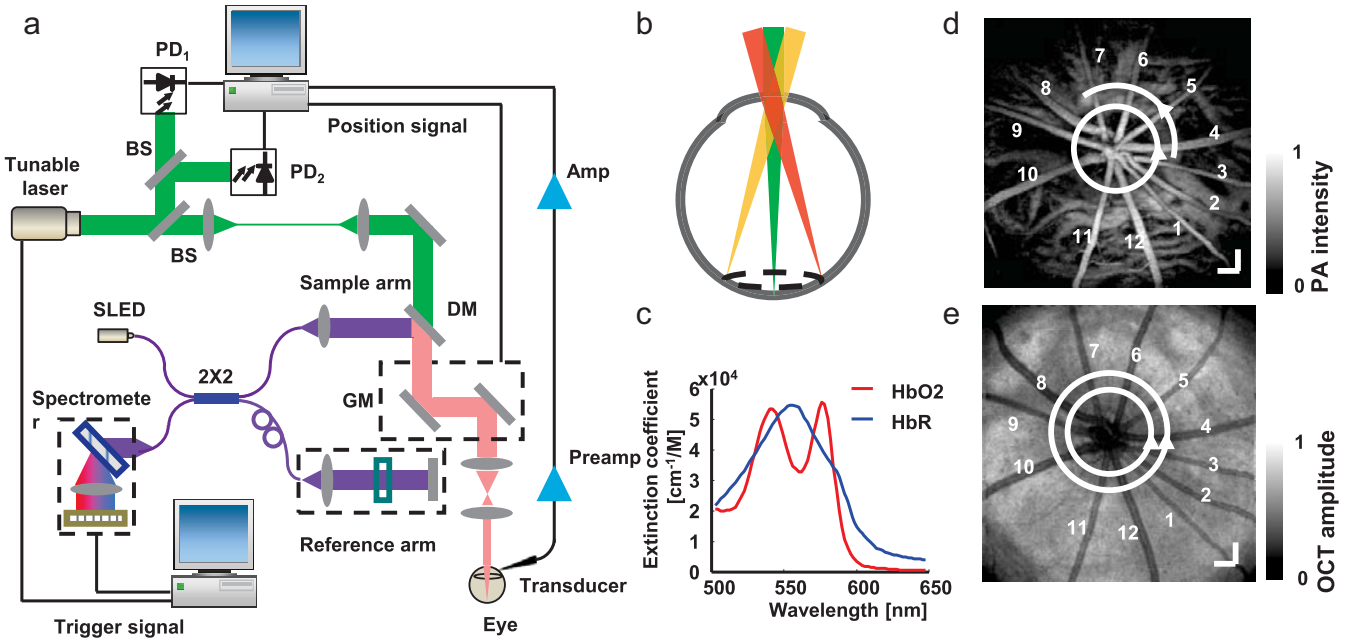

Figure 1 | Illustration of integrated PAOM and SD-OCT to measure rMRO$_2$. (a) Schematic of the experimental setup. (b) Circular scanning pattern on the retina. (c) Molar extinction coefficient spectrum of oxy- and deoxy-hemoglobin. (d) A maximum-amplitude-projection PAOM fundus image showing 12 major retinal vessels. The circle (radius: 0.45 mm) and the concentric arc (radius: 0.56 mm) are scanning trajectories from which PAOM B-scan images were acquired for assessing sO$_2$. Bar: 200 μm. (e) An OCT fundus image of the same rat showed in the panel d. The circles (radii of 0.45 and 0.56 mm) highlight the scanning trajectories for measuring Doppler angle and blood flow. Bar: 200 μm.

selected illumination wavelengths. Hickham *et al.* first applied two-wavelengths fundus photography to map retinal sO$_2$[18], yet two-wavelength fundus photography is sensitive to light scattering and is easily affected by retinal local parameters such as vessel size, melanin concentration in retinal pigment epithelium[16]. To improve the stability and accuracy in sO$_2$ measurement, researchers employed additional wavelengths in fundus photography in later studies to compensate for the effect of optical scattering, as well as the vessel size[19–22]. In addition, researchers chose wavelengths 548 nm and 610 nm to correct the influence of melanin based on the approximate linearly decreased extinction coefficient of melanin within this wavelength range[23]. Building on such modifications, the performance of retinal oximetry was much improved. However, adding more wavelengths cannot completely eliminate the influence from optical scattering and variations of retinal local parameters[16]. Our recent numerical simulation study demonstrated that the absolute measured sO$_2$ error could be up to be 20% when the vessel size is as large as 160 μm or the melanin concentration in the retinal pigment epithelium is as high as 8 mmol/L[24].

Optical coherence tomography (OCT) has the potential to measure retinal sO$_2$ measurement[25,26] noninvasively. We recently explored the feasibility of using visible-light OCT (Vis-OCT) to quantify retinal sO$_2$ *in vivo*[27]; yet there is still a long way before OCT can be verified to precisely measure sO$_2$ at various anatomical sites. The capability of photoacoustic (PA) imaging to quantify sO$_2$, however, has been well-studied and well-documented in various anatomical sites, including the ears[28], esophagus, colon[29], and brain[30].

Building on the proven strength of PA imaging[31], we developed photoacoustic ophthalmoscopy (PAOM) to address the aforementioned need in retinal metabolic imaging using rats as an animal model. We further optimized a multi-wavelength methodology in PAOM to quantify retinal sO$_2$.

Results

Imaging schematic for both sO$_2$ and flow quantification. We accessed rMRO$_2$ by integrating PAOM with Doppler SD-OCT. Figure 1a illustrates the combined functional imaging system (see Online Methods for more details.). The aligned and collimated probing beams for both PAOM and SD-OCT were scanned by the same optics on the retina for imaging. We employed a circular scanning pattern centered at the optic disc to image all the retinal vessels within single B-scans as shown in Figure 1b. The molar extinction coefficients of oxy-hemoglobin (HbO$_2$) and deoxy-hemoglobin (HbR) can be found in Figure 1c, based on which sO$_2$ can be measured by multi-wavelength PAOM. The accuracy of PAOM was validated by measuring a series of *ex vivo* bovine blood (Quad Five Inc, Ryegate, MO) phantom samples with different preset sO$_2$ levels (see Supplementary Figure S1 and Supplementary Table S1 for more details). A typical anatomical fundus image acquired by PAOM is shown in Figure 1d (see Supplementary Figure S2 for 3D visualization). In Figure 1d, the white circle and arc were scanning trajectories, from where PA signals were extracted for sO$_2$ measurement. To obtain retinal blood flow, we employed dual-beam scanning in SD-OCT. Corresponding SD-OCT fundus image is shown in Figure 1e; where the two white circles highlight the scanning trajectories used to measure Doppler angle and phase.

Quantification of retinal sO$_2$ by muti-wavelength PAOM. The steps to measure sO$_2$ using multi-wavelength PAOM are illustrated in Figure 2. We scanned along the highlighted circular trajectory around the optic disk at three wavelengths (570, 578, and 588 nm). Scanning around the optic disk enabled us to measure the complete hemodynamic properties of the eye from a fast one-dimensional scan. The B-scan images along the circular trajectory at the three-wavelengths are shown in the top part of Figure 2a. Fluctuations of the vessels' position along the vertical direction reflect the distances from the vessels to the ultrasonic detection. The PA amplitudes of the 12 major vessels were extracted and are shown below their corresponding B-scan images. We then used the multi-wavelength PA amplitudes of the vessels to estimate sO$_2$ in every vessel based on the molecular extinction coefficients of HbO$_2$ and HbR at corresponding optical wavelengths (Figure 1c). The steps to extract

vessel PA amplitude from B-scan images are detailed in Supplementary Figure S3. After inverse calculation, the sO_2 values of all the highlighted vessels scanned along the circular trajectory are given in Figure 2b and Figure 2c. On average, our results show the sO_2 values in arterial and venous blood to be 93.0 ± 3.5% and 77.3 ± 9.1%, respectively. Shonat et al. pioneered the measuring of retinal oxygen partial pressure (PO_2) based on phosphorescence quenching techniques in cats[32]. They reported that the cat's venous PO_2 was 30 Torr, which corresponded to a 42% sO_2 based on the oxygen-hemoglobin dissociation curve in cat[33]. Their measurements were consistent with other reported results in cats[33]. Different animal models are shown to have different retinal oxygenations[34,35]; the rodent's venous sO_2 was reported to be around 70%[36,37], which agrees with our PAOM measurements.

Spatial consistency in sO_2 measurements along the same vessels is essential, but it was not successfully demonstrated in existing retinal oximetry due to influences from retinal vessel diameter and retinal pigmentation variation[16,24]. We tested our spatial consistency by comparing sO_2 measurements from four selected vessels scanned at different positions from the optic disk, as highlighted in Figure 1d. The radii of the two circles were 0.45 mm and 0.56 mm, a separation that is small enough where sO_2 values at the two locations should be the same in each vessel. Results shown in Figure 2d confirm such consistencies, with the largest absolute variation found to be 3.9%.

Quantification of retinal flow by Doppler SD-OCT. Figure 3 shows the steps to quantify retinal blood flow velocity and vessel diameter using Doppler SD-OCT[38,39]. Because Doppler SD-OCT can only access the projected blood flow velocity along the probing beam, the Doppler angle (defined as the angle between the vessel and the probing beam) is required to estimate the absolute velocity. We adopted the dual-ring scanning method[38,39] used by several groups to determine the Doppler angle (see Supplementary Figure S4). The two circular trajectories overlapping with those in PAOM are highlighted in the OCT fundus image (Figure 1e). The OCT B-scan amplitude and phase images (before bulk motion correction) from the inner scanning trajectory are shown in Figure 3a, and Figure 3b, respectively. We obtained the blood flow velocity in each vessel based on the calculated OCT phase variations and their corresponding Doppler angles.

Figure 3c shows a magnified view of the imaged blood flow velocity distribution in a typical vessel (highlighted by the arrow in Figure 3b). The laminar flow profile along the vessel's horizontal centerline clearly shows a quadratic dependence on radii within the vessel. Figure 3d provides the overall measurements of blood flow velocities in this particular retina, from which we can observe higher velocities in arteries than veins. We also extracted the vessel diameter from SD-OCT phase images using a recently developed automatic segmentation algorithm[40], with results given in Figure 3e. The vessel diameters are shown in Figure 3e, where the veins have larger diameters than the arteries. By multiplying blood velocity with vessel cross-sessional size, we can calculate total retinal blood flow as 7.43 ± 0.51 μl/minute and 7.38 ± 0.78 μl/minute within the venous and arterial systems, respectively (Figure 3f). The results are consistent with previously reported results[41] and the venous and arterial blood flows match each other well.

Quantification of $rMRO_2$. With sO_2 and blood flow acquired, the $rMRO_2$ can be, therefore, calculated. For the particular retina whose sO_2 and flow we present in Figure 2 and Figure 3, the measured $rMRO_2$ of the complete inner retina is 373.41 ± 88.04 ng/minute, or 297.86 ± 70.23 nl/minute. This is lower than the 499 nl/minute measured by Shahidi et al[42]. As they pointed out, their $rMRO_2$ result was higher than other reported values[42], which was suggested to be caused by measurement variations in some important parameters,

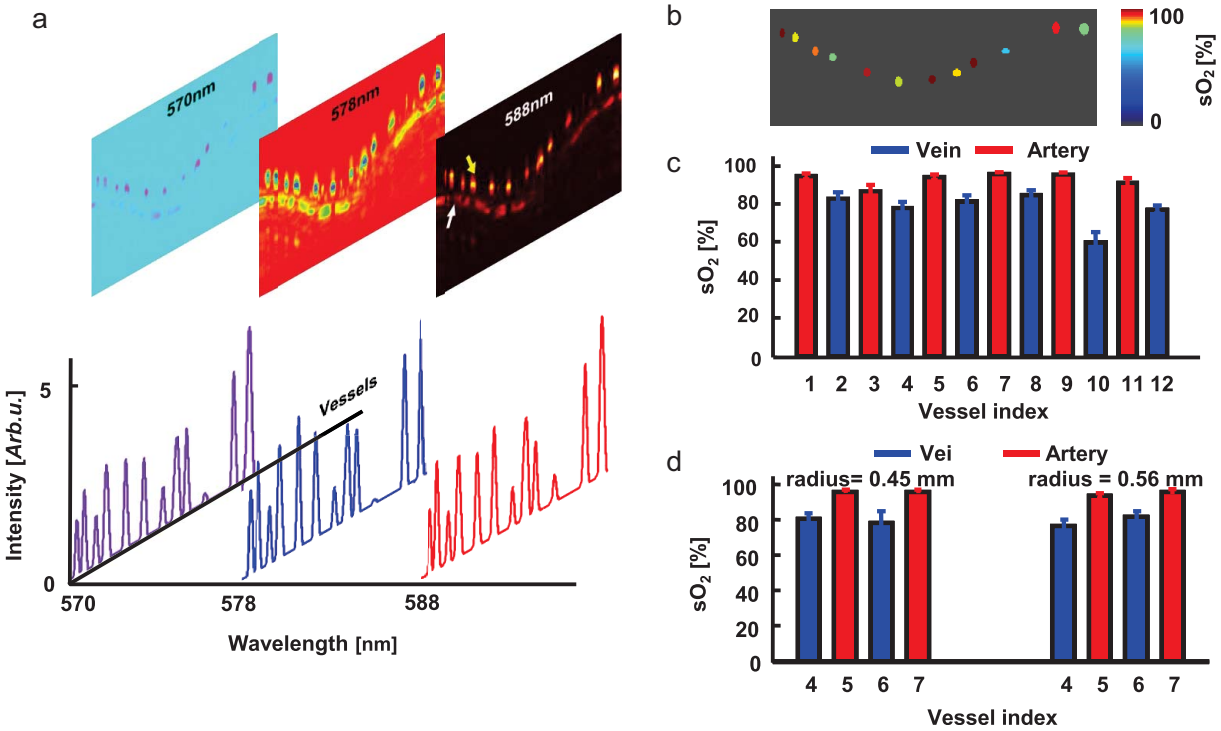

Figure 2 | Steps to quantify retinal sO_2 using multi-wavelength PAOM. (a) Cross-sectional retina image acquired at 578 nm, 580 nm, and 588 nm illuminating wavelengths. Top: raw PAOM B-scan images in pseudo-colors. In the 588-nm image, the yellow arrow highlights retinal blood vessels and the white arrow highlights choroidal vessels. Bottom: PA amplitudes of the 12 vessels. (b) pseudo-colored vessels as imaged in the circular PAOM B-scan based on their measured sO_2 values; (c) comparison of sO_2 values in all major vessels. (d) Measured sO_2 in selected vessels from different radii as shown in Figure 1b, where spatial consistency is demonstrated.

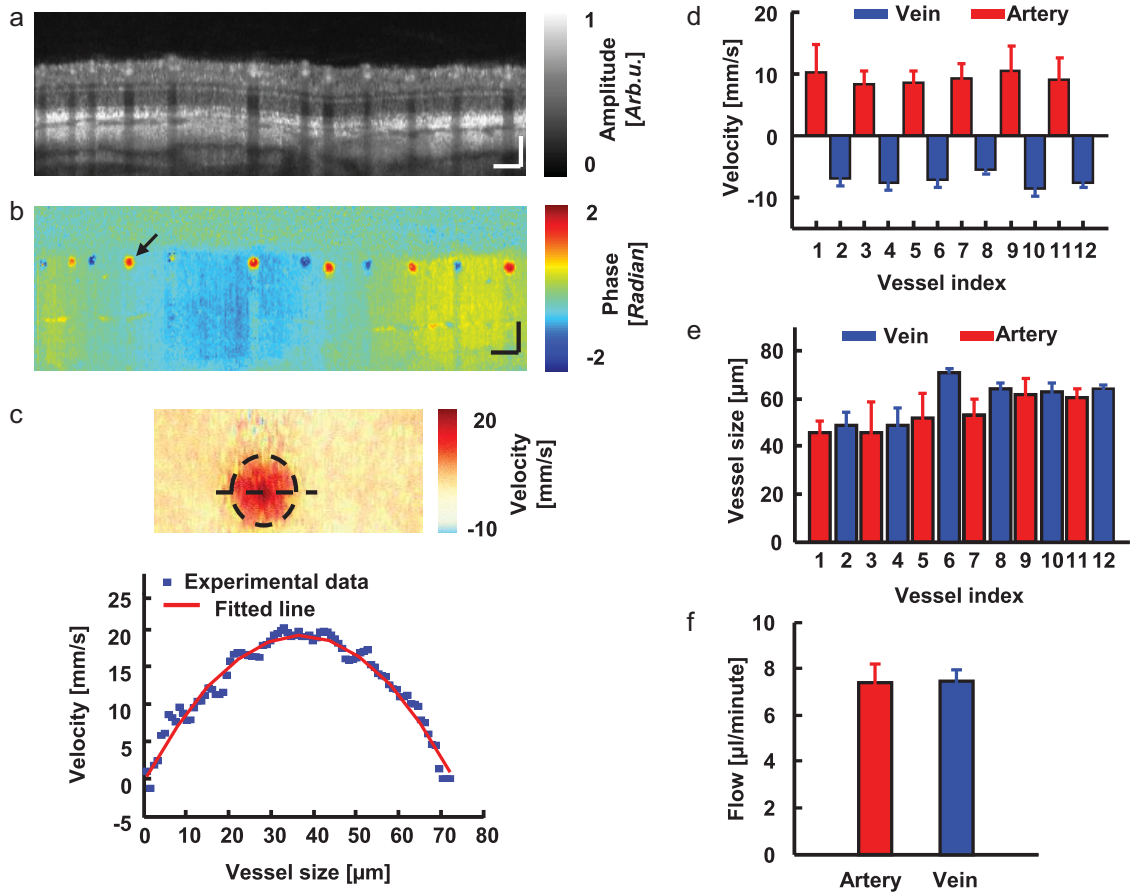

Figure 3 | Steps to measure retinal blood flow using SD-OCT. (a) OCT B-scan amplitude image acquired from the inner circle as shown in Figure 1c. (b) OCT B-scan phase image from the inner circle. (c) Blood velocity distribution within the vessel highlighted by the black arrow in panel b. Top: two-dimensional distribution along the vessel cross-section; Bottom: experimental and fitted transverse velocity profiles along the horizontal position highlighted by the dashed line. (d) Average blood flow velocity in all the major retinal vessels. The positive velocity of arterial blood shows flow coming from the optic disk to peripheral areas; the negative velocity of venous blood indicates flow coming from peripheral areas to the optic disk. (e) Calculated vessel diameters of all the major retinal vessels. (f) Comparison of the measured total arterial and venous blood flows.

such as the retinal mass. In their results, the venous sO_2 was around 50% (after converting the oxygen partial pressure into sO_2 value based on the dissociation curve), which was lower than the reported normal rodent venous sO_2 value of around 70%[36]. Also, their measured total retinal blood flow in the inner retina was 10.06 μl/min, which was higher than other reported values[43]. We think that different anesthesia conditions may also contributed to the discrepancy between our and Shahidi's measurements.

Discussion

Compared with other reported retinal functional imaging modalities, our integrated PAOM and Doppler SD-OCT approach to measure $rMRO_2$ is advantageous in several aspects. First, our method completely interrogates $rMRO_2$ noninvasively. Most of the currently reported retinal functional imaging methods[13,16,39,41] can measure only one functional parameter, either retinal sO_2 or blood flow, which is insufficient for $rMRO_2$ quantification; other proposed imaging modalities that can quantify $rMRO_2$ are invasive[42], which is not suitable for *in vivo* applications. Secondly, PAOM is expected to assess retinal sO_2 much more accurately than the multi-wavelength fundus photography[24].

Our simulation studies suggested that such an improvement originates from the better quantification of blood optical absorption by PAOM than the multi-wavelength fundus photography[24]. Fundus photography estimates light absorption within blood from the collected retinal light reflectance[16]. Several factors deteriorated the accuracy of the indirect light absorption measurement. First, the acquired reflected light from the vessel is a superposition of photons, which may have no interaction, partial, or full interaction (travelled through the entire vessel) with the retinal blood. Among these photons, only fully interacted photons can provide accurate measurement of the optical absorption by blood[24]. Secondly, photons backscattered from the vessel's neighboring areas interact more (scattering/absorption) with the melanin in the retinal pigment epithelium (RPE) layer than photons reflected from vessels, because high absorption or scattering by blood allows only a few photons to enter into the RPE. Additional details on how scattering affects fundus photography measurements can be found in our previous Monte Carlo simulation studies[24].

For multispectral PAOM, the imaging contrast is based on optical absorption from blood or RPE melanin within the visible light spectral range[31]. The absorbed photons can be either ballistic or scattered photons. In the current study, the time-resolved light induced acoustic signals can provide axial resolution of up to 23 μm, which enables us to separate the signals of retinal blood vascular from the RPE melanin given the retina thickness is around 200 μm[44]. As a result, PAOM signals generated from major vessels can be considered to be mainly generated from hemoglobin. Optical scattering, however, does affect the resolution of PAOM. It's reported that the lateral resolution can be degraded by 14% in turbid media compared with the case of no scattering when the imaging depth is close to the transport mean free path[45]. In PAOM, the theoretical lateral resolu-

tion is estimated to be 20 μm. Considering a 14% degradation, the lateral resolution will be reduced to 22.8 μm. Since the degradation in lateral resolution is merely 10% of the theoretical lateral resolution, it may not influence our experimental results much. In addition, the rat eye is notable for its stronger chromatic aberration[46,47], we analyzed the chromatic aberration effects on the PAOM image within a bandwidth as short as 18 nm, and it turned out the chromatic effects on imaging is small, and should not affected the accuracy of PAOM results (see Supplemental Figure S5 for more details.)

Although versatile and unique, the combined PAOM and SD-OCT imaging system has the following limitations. One major concern comes from ultrasonic signal detection. First, ultrasonic signal detection requires physical contact, as in the experiment, where we coupled a needle ultrasonic transducer to the rodent eyelid with ultrasonic gel[48]. This ultrasonic signal detection scheme is not preferred in clinical settings. Second, the large size and opacity of the needle ultrasonic piezoelectric detector requires a long working distance, which forces a small NA for OCT and thus limits its imaging quality[48]. To overcome this, we recently developed a transparent micro-ring resonator for ultrasonic signals detection, which has a physical dimension of a few millimeters and a much lower noise equivalent pressure[49]. We plan to fabricate this micro-ring resonator onto a contact lens serving as the ultrasonic detector, which requires no ultrasonic gel coupling and allows for a flexible working distance. Thirdly, visual stimulus is reported to increase the retinal vessel diameter and blood flow, as well as affect the retinal sO_2 through the process of retinal neurovascular coupling[43,50]. These may affect the accuracy of the PAOM. It has been demonstrated that the neurovascular coupling depends on visual stimulus frequency and stimulus duration[51], where the examined flickering frequency, within our understanding, ranged from 10 to 60 Hz with a typical stimulation time last more than 10 s. Such a condition does not exist in PAOM, where we used 25-kHz A-line rate and 2.5 s total illumination time at each illuminating wavelength. Whether each PAOM illumination will introduce effective neurovascular coupling and lead to an observable hemodynamic response within each acquisition needs further investigation in the future. Lastly, despite the good match between measured sO_2 by PAOM and the preset sO_2 in blood phantom experiments (Supplemental Figure S1), we also understand that the phantom experimental conditions are different from those in *in vivo* rodent experiments. For example, there are eye movements during imaging, aberration from the eyeball, etc. Whether such differences will affect the sO_2 quantification or not also require more future validation.

Another concern is that the performance of dual-ring scanning SD-OCT may be influenced by eye movement due to the consecutive and non-simultaneous scanning sequence of the small and big ring. In our present study, we averaged the vessels' central positions across eight pairs of small-big scanning patterns to prevent motion-induced variation. A motion-insensitive alternative is to scan a pair of small and big rings simultaneously[38], which, further complicates the imaging system. Also, we measured the vessel diameter axially because OCT offers higher axial resolution than lateral resolution, and we calculated the vessel cross-sectional area using the axial diameter by assuming a cylindrical vessel profile as other researchers did[52].

Dysfunctions in the oxygen metabolic rate (MRO_2) are not merely limited to the retina, as MRO_2 also has been found to be involved in other diseases, such as cancer[53], Alzheimer's disease[54], and heart failure[55]. Owing to its capability to accurately assess MRO_2, our multimodal imaging technology can help better understand a wider spectrum of disease mechanisms beyond blinding diseases.

Methods

Experimental setup. A schematic of the experimental setup is shown in Figure 1a. We used a tunable dye laser (Cobra, Sirah Laser and Plasmatchnik GmbH) pumped by a pulsed Nd:YLF laser (IS8II-E, Edge-Wave GmbH; pulse duration: 5 ns) as the illumination source for PAOM. The tunable laser output was collimated into 2 mm in diameter, then merged with the light of SD-OCT (center wavelength: 840 nm; bandwidth: 50 nm; SLED IPSDD0804, InPhenix). A two-dimensional galvanometer scanned the combined light beams (QS-7, Nutfield Technology) and relayed them to the eye through a telescopic lenses system. In PAOM, acoustic waves induced by light absorption were detected by an unfocused small-footprint ultrasonic transducer (central frequency: 40-MHz; bandwidth: 30-MHz; active element size: 0.5 × 0.5 mm^2) attached to the rat's eyelid through ultrasonic gel. The detected photoacoustic signals were amplified by two amplifiers (ZFL-500LN+, Mini-circuits, and 5073PR, Olympus, total gain: 60 dB) and digitalized by a data acquisition card (CS14200, Gage Applied Technology) at a sampling rate of 200 MS/s. In SD-OCT, backscattered light from the retina first interfered with the reference arm light, then sampled by a home-made spectrometer at an A-line rate of 25-kHz. The lateral resolutions of both PAOM and SD-OCT were around 20 μm in the retina with a slight difference caused by the different spectral ranges. The axial resolutions of PAOM and OCT were 23 μm and 5.6 μm, respectively[56].

During imaging, a 256 × 256 A-lines scanning pattern was employed to acquire fundus images in both SD-OCT and PAOM. The circular B-scanning (each B-scan contains 4096 A-lines, A-line rate 25-kHz) was used for flow and sO_2 measurement. In Doppler OCT, we performed eight pairs of big-small circular scans. We confirmed that 25-kHz A-line rate is able to precisely assess retinal blood flow by comparing the measurement at 25-kHz with results acquired by a 70-kHz A-line rate OCT, which is considered sufficiently high to acquire the entire pulsatile flow profile[57].(see Supplementary Figure S6 for more details). In PAOM, the illuminating laser energy was 40 nJ/pulse, which is considered eye-safe as detailed in Supplementary Materials. For sO_2 detection, at each wavelength, we scanned 16 consecutive circles centered on optical disc with 4096 A-lines in each circle. The time-resolved photoacoustic signals were collected in each A-line. After data collection, we first reconstructed the 16 B-scan images at each wavelength and then sequentially estimated the sO_2 from the 1st B-scan to the 16th B-scan. Finally, all the sO_2 measurements for each vessel were averaged across the 16 B-scan results.

Animal Preparation. We used wild-type rats (Sprague Dawley, 300 g, Harlan Laboratories, Indianapolis, IN) in our studies. During experiments, a mixture of isoflurane and normal air was supplied to the rats through a commercial non-rebreathing ventilating system (Vaporizer Inc, Rockmart, GA). We first placed the rat into an induction chamber and adjusted the vaporizer to 2% isoflurane vapor output percentage, setting the attached gas flowmeter at 3 L/min. The vaporizer and flowmeter setting corresponded to 12 mL/hour anesthetic agent gas consumption and were maintained for 10 minutes; then changed to 1.5% isoflurane and 2 L/min air flow for additional five minutes, corresponding to 6.6 mL/hour anesthetic agent gas consumption. At this point, the rat was under deep anesthesia. We then placed the rat on a homemade adjustable holder for imaging. The homemade holder was connected to the ventilation system, which kept the rat ventilated at the rate corresponding to 6.6 mL/hour isoflurane gas consumption. We dilated the rats' pupils with a 1% Tropicamide ophthalmic solution and paralyzed the iris sphincter muscle with a 0.5% Tetracaine hydrochloride ophthalmic solution. Meanwhile, artificial teardrops (Systane, Alcon Laboratories, Inc.) were applied every other minute to prevent corneal dehydration. During the experiment, the rats' electrocardiogram was monitored (ETH-256 Amplifier, Iworx). Their blood oxygen saturation levels were measured to be around 90% and the heart rate was measured to be around 223 bpm (Pulse oximetry, Model 8500AV, Nonin Medical, Inc).

All experimental procedures were in compliance with ARVO Statement for the Use of Animals in Ophthalmic and Vision Research, and laboratory animal protocol approved by the Institutional Animal Care and Use Committee at Northwestern University.

sO_2 quantification. We selected three wavelengths (570, 578, and 588 nm) for sO_2 imaging in PAOM. The sO_2 value of each vessel was estimated as follows:

$$sO_2(x,y,z) = \frac{[HbO_2]_{(x,y,z)}}{[HbO_2]_{(x,y,z)} + [HbR]_{(x,y,z)}}, \quad (1)$$

where [HbR] and [HbO_2] are the concentrations of oxy- and deoxy-hemoglobin [g/L]. [HbR] and [HbO_2] were quantified through optical absorption by retinal blood. The blood absorption coefficient can be expressed as

$$\mu_a(\lambda_i) = \varepsilon_{HbR}(\lambda_i)\cdot[HbR] + \varepsilon_{HbO_2}(\lambda_i)\cdot[HbO_2], \quad (2)$$

where $\varepsilon_{HbR}(\lambda_i)$ and $\varepsilon_{HbO_2}(\lambda_i)$ are the known molar extinction coefficients [$cm^{-1}M^{-1}$] of HbR and HbO_2 at wavelength λ_i [nm], respectively. In PAOM, the detected PA amplitude pa(x, y, z, λ_i) is considered to be proportional to the local optical energy deposition $\phi(x, y, z, \lambda_i)$, which is a product of local $\mu_a(x, y, z, \lambda_i)$ and local optical fluence $F(x, y, z, \lambda_i)$. Thus, Eq. 2 can be rewritten as:

$$\begin{aligned} \mathrm{pa}(\lambda_i,x,y,z) &= K_1\cdot\varphi(\lambda_i,x,y,z) \\ &= K_1\cdot F(x,y,z,\lambda_i)\cdot(\varepsilon_{HbR}(\lambda_i)\cdot[HbR] + \varepsilon_{HbO_2}(\lambda_i)\cdot[HbO_2]), \end{aligned} \quad (3)$$

where K_1 is the proportionality coefficient. By assuming consistent optical illumination and ignoring optical attenuation in the retina, we can consider

$F(x, y, z, \lambda_i)$ to be constant and simplify $K_1 \cdot F(x, y, z, \lambda_i)$ as K_2. For multiple wavelength PA measurements, Eq. 3 becomes

$$\mathrm{PA} = K_2 M H \tag{4}$$

where $M = \begin{bmatrix} \varepsilon_{HbR}(\lambda_1) & \varepsilon_{HbO_2}(\lambda_1) \\ \vdots & \vdots \\ \varepsilon_{HbR}(\lambda_n) & \varepsilon_{HbO_2}(\lambda_n) \end{bmatrix}$, $H = \begin{bmatrix} [HbR] \\ [HbO_2] \end{bmatrix}$, and $\mathrm{PA}(x,y,z) = \begin{bmatrix} \mathrm{pa}(\lambda_1,x,y,z) \\ \vdots \\ \mathrm{pa}(\lambda_n,x,y,z) \end{bmatrix}$. Although $[HbR]$ and $[HbO_2]$ can only be estimated as relative values, the final sO_2 in Eq. 1 is an absolute value[58].

In order to minimize the influence of the spatial sensitivity distribution of the unfocused transducer, the PA signals of each vessel at the 578 nm and 588 nm optical illuminations were normalized by the PA amplitude of the same vessel acquired at the isosbestic wavelength of 570 nm.

Vessel diameter and cross section area measurements. We measured the vessel diameter axially in the OCT B-scan amplitude image, because of the high axial resolution of OCT. If we denote the vessel diameter in the B-scan as *Dia* [m], the actual vessel diameter *Dia_r* [m] is

$$Dia\_r = Dia \times \sin(\theta) \tag{5}$$

where θ [radians] is the Doppler angle. The vessel cross-sectional area A [m^2] is calculated by

$$A = \pi \times \frac{Dia\_r^2}{4}. \tag{6}$$

Blood velocity and flow rate

In Doppler OCT, the probing light passes through the pupil lens and is focused onto retinal vessels. The blood velocity v [m/s] can be calculated as

$$v = \frac{f_{sample} \cdot \lambda_0 \cdot \Delta\phi}{4 \cdot \pi \cdot n \cdot \cos(\theta)}, \tag{7}$$

where f_{sample} [kHz] is the SD-OCT A-line rate; λ_0 [nm] is the center wavelength of the SD-OCT light source; $\Delta\Phi$ is the phase shift [degree] between adjacent OCT A-lines after bulk motion correction[59]; n [dimensionless] is the refractive index of the sample (n = 1.4); and θ [radians] is the Doppler angle (estimation of the Doppler angle can be found in Supplementary Figure S4). To reduce the influence of eye motion on Doppler angle estimation, we averaged the estimated vessel depth across eight consecutive OCT B-scans. In our current work, the largest error in vessel depth is 2.9 μm across eight B-scans. Considering the scanning radii difference between the outer- and inner-scanning rings is 110 μm, the largest 2.9 μm depth error results in an angle estimation error of 1.5 degrees. Since the mean value of the measured Doppler angle is around 82 degrees, the influence of the 1.5-degree angle error is small.

We observed the phase-wrap in retinal flow measurement. Phase-wrap can be corrected once we know the axial blood flow direction, which can be obtained from the phase value close to the vessel border since flow velocity near vessel wall is small enough to prevent phase-wrapping[60]. With the known blood flow direction and assuming the actual phase $\Delta\varphi < 0$, we have

$$\Delta\phi = \begin{cases} \Delta\phi, & \Delta\phi < 0 \\ \Delta\phi - 2\cdot\pi, & \Delta\phi > 0 \end{cases} \tag{8}$$

after phase wrapping correction. If the actual phase is $\Delta\phi > 0$, we have

$$\Delta\phi = \begin{cases} \Delta\phi, & \Delta\phi > 0 \\ \Delta\phi + 2\cdot\pi, & \Delta\phi < 0 \end{cases} \tag{9}$$

after phase wrapping correction. After the blood velocity and vessel size are obtained, the blood flow in the i_{th} vessel is

$$F_i = v_i \times A_i, \tag{10}$$

where v_i is the average velocity and A_i is the vessel cross-sectional area.

Retinal metabolic rate of oxygen (rMRO₂). The $rMRO_2$ [g/min] is quantified as

$$\begin{aligned} rMRO_2 &= \frac{60 \times 4 \times W_{O2}}{W_{HbO2}} \times [HbT] \times (sO_{2a} \times F_a - sO_{2v} \times F_v) \\ &= \frac{60 \times \pi \times W_{O2}}{W_{HbO2}} \times [HbT] \times \left(\sum_{i=1}^{M} sO_{2ai} \times d_{ai}^2 \times v_{ai} - \sum_{i=1}^{N} sO_{2vi} \times d_{vi}^2 \times v_{vi}\right), \end{aligned} \tag{11}$$

where W_{O2} and W_{HbO2} are the molecular weights of O_2 and oxyhemoglobin, which are 32 and 68000 [g/mol], respectively; [HbT] is the total concentration of hemoglobin in the rat, which is 150 [g/L] in current studies; sO_{2ai} and sO_{2vi} are sO_2 values in the i_{th} artery and vein, respectively; d_{ai} and d_{vi} are the vessel diameter of i_{th} artery and vein, respectively; v_{ai} and v_{vi} are the blood flow velocity within the i_{th} artery and vein, respectively; M and N are the number of arteries and veins, respectively. The standard deviation of $rMRO_2$ [g/min] (*rMRO₂_std*) is derived through the principle of error propagation as follows.

$$\begin{aligned} rMRO_2\_std = \frac{60 \times \pi \times W_{O2}}{W_{HbO2}} \times [HbT] \times sqrt\Big(\sum_{i=1}^{N} &((std(sO_{2ai}) \times d_{ai}^2 \times v_{ai})^2 \\ &+ (2 \times d_{ai} \times std(d_{ai}) \times sO_{2ai} \times v_{ai})^2 + (d_{ai}^2 \times sO_{2ai} \times std(v_{ai}))^2) \\ &+ \sum_{i=1}^{M} ((std(sO_{2vi}) \times d_{vi}^2 \times v_{vi})^2 + (2 \times d_{vi} \times std(d_{vi}) \times sO_{2vi} \times v_{vi})^2 \\ &+ (d_{vi}^2 \times sO_{2vi} \times std(v_{vi}))^2)\Big) \quad , \end{aligned} \tag{12}$$

where $std(\cdot)$ denotes the standard deviation operator and $sqrt(\cdot)$ denotes the square root operator. The unit of $rMRO_2$ in Eq. 11 and Eq. 12 is ng/min, and we can convert ng/min to L/min by

$$V = n_g \times R \times T / P, \tag{13}$$

where V is the volume of gas; n_g is the number of moles of gas; R is 8.3145 [$J \cdot mole^{-1} \cdot K^{-1}$]; T is the blood temperature (311.15 K); and P is the standard atmospheric pressure (101,325 Pa). All measured data, including vessel size, sO_2, and flow velocity, are given in Supplemental Table S2.

1. Congdon, N. *et al.* Causes and prevalence of visual impairment among adults in the United States. *Arch. Ophthalmol.* **122**, 477–485 (2004).
2. Pascolini, D. & Mariotti, S. P. Global estimates of visual impairment: 2010. *Br. J. Ophthalmol.* **96**, 614–618 (2012).
3. Yu, D. Y. & Cringle, S. J. Oxygen distribution and consumption within the retina in vascularised and avascular retinas and in animal models of retinal disease. *Prog. Retin. Eye Res.* **20**, 175–208 (2001).
4. Yu, D. Y. & Cringle, S. J. Retinal degeneration and local oxygen metabolism. *Exp. Eye Res.* **80**, 745–751 (2005).
5. Tezel, G. & Wax, M. B. Hypoxia-inducible factor 1α in the glaucomatous retina and optic nerve head. *Arch. Ophthalmol.* **122**, 1348–1356 (2004).
6. Kohner, E. M., Patel, V. & Rassam, S. M. Role of blood flow and impaired autoregulation in the pathogenesis of diabetic retinopathy. *Diabetes* **44**, 603–607 (1995).
7. Antonetti, D. A., Klein, R. & Gardner, T. W. Diabetic retinopathy. *N. Engl. J. Med.* **366**, 1227–1239 (2012).
8. Ciulla, T. A. *et al.* Color Doppler imaging discloses reduced ocular blood flow velocities in nonexudative age-related macular degeneration. *Am. J. Ophthalmol.* **128**, 75–80 (1999).
9. Riva, C. E., Grunwald, J. E. & Sinclair, S. H. Laser Doppler Velocimetry study of the effect of pure oxygen breathing on retinal blood flow. *Invest. Ophthalmol. Vis. Sci.* **24**, 47–51 (1983).
10. Hickam, J. B., Sieker, H. O. & Frayser, R. Studies of retinal circulation and A-V oxygen difference in man. *Trans. Am. Clin. Climatol. Assoc.* **77**, 34–44 (1960).
11. An, L. & Wang, R. K. In vivo volumetric imaging of vascular perfusion within human retina and choroids with optical micro-angiography. *Opt. Express* **16**, 11438–11452 (2008).
12. Wangsa-Wirawan, N. D. & Linsenmeier, R. A. Retinal oxygen: fundamental and clinical aspects. *Arch. Ophthalmol.* **121**, 547–557 (2003).
13. Berkowitz, B. A. & Wilson, C. A. Quantitative mapping of ocular oxygenation using magnetic resonance imaging. *Magn. Reson. Med.* **33**, 579–581 (1995).
14. De La Garza, B. H., Muir, E. R., Li, G., Shih, Y. Y. & Duong, T. Q. Blood oxygenation level-dependent (BOLD) functional MRI of visual stimulation in the rat retina at 11.7 T. *NMR Biomed.* **24**, 188–193 (2011).
15. Duong, T. Q. Magnetic resonance imaging of the retina: A brief historical and future perspective. *Saudi J Ophthalmol.* **25**, 137–143 (2011).
16. Harris, A., Dinn, R. B., Kagemann, L. & Rechtman, E. A review of methods for human retinal oximetry. *Ophthalmic. Surg. Lasers Imaging* **34**, 152–164 (2003).
17. Prahl, S. Optical absorption of Hemoglobin. <http://omlc.org/spectra/hemoglobin/>, (1999) Date of access: 04/05/2013.
18. Hickam, J. B., Frayser, R. & Ross, J. C. A study of retinal venous blood oxygen saturation in human subjects by photographic means. *Circulation* **27**, 375–386 (1963).
19. Delori, F. C. Noninvasive technique for oximetry of blood in retinal vessels. *Appl. Opt.* **27**, 1113–1125 (1988).
20. Vucea, V., Bernard, P. J., Sauvageau, P. & Diaconu, V. Blood oxygenation measurements by multichannel reflectometry on the venous and arterial structures of the retina. *Appl. Opt.* **50**, 5185–5191 (2011).
21. Hardarson, S. H. *et al.* Automatic retinal oximetry. *Invest. Ophthalmol. Vis. Sci.* **47**, 5011–5016 (2006).
22. Traustason, S. *et al.* Spectrophotometric retinal oximetry in pigs. *Invest. Ophthalmol. Vis. Sci.* **54**, 2746–2751 (2013).
23. Hammer, M., Vilser, W., Riemer, T. & Schweitzer, D. Retinal vessel oximetry-calibration, compensation for vessel diameter and fundus pigmentation, and reproducibility. *J. Biomed. Opt.* **13**, 054015 (2008).
24. Liu, W., Jiao, S. & Zhang, H. F. Accuracy of retinal oximetry: a Monte Carlo investigation. *J. Biomed. Opt.* **18**, 066003 (2013).

25. Yi, J. & Li, X. Estimation of oxygen saturation from erythrocytes by high-resolution spectroscopic optical coherence tomography. *Opt. Lett.* **35**, 2094–2096 (2010).
26. Faber, D. J., Mik, E. G., Aalders, M. C. & van Leeuwen, T. G. Toward assessment of blood oxygen saturation by spectroscopic optical coherence tomography. *Opt. Lett.* **30**, 1015–1017 (2005).
27. Yi, J., Wei, Q., Liu, W., Backman, V. & Zhang, H. F. Visible-light optical coherence tomography for retinal oximetry. *Opt. Lett.* **38**, 1796–1798 (2013).
28. Yao, J., Maslov, K. I., Zhang, Y., Xia, Y. & Wang, L. V. Label-free oxygen-metabolic photoacoustic microscopy in vivo. *J. Biomed. Opt.* **16**, 076003 (2011).
29. Yang, J. M. *et al*. Simultaneous functional photoacoustic and ultrasonic endoscopy of internal organs in vivo. *Nat. Med.* **18**, 1297–1302 (2012).
30. Hu, S., Maslov, K., Tsytsarev, V. & Wang, L. V. Functional transcranial brain imaging by optical-resolution photoacoustic microscopy. *J. Biomed. Opt.* **14**, 040503 (2009).
31. Zhang, H. F., Maslov, K., Stoica, G. & Wang, L. V. Functional photoacoustic microscopy for high-resolution and noninvasive in vivo imaging. *Nat. Biotechnol.* **24**, 848–851 (2006).
32. Shonat, R. D., Wilson, D. F., Riva, C. E. & Pawlowski, M. Oxygen distribution in the retinal and choroidal vessels of the cat as measured by a new phosphorescence imaging method. *Appl. Opt.* **31**, 3711–3718 (1992).
33. Herbert, D. A. & Mitchell, R. A. Blood gas tensions and acid-base balance in awake cats. *J. Appl. Physiol.* **30**, 434–436 (1971).
34. Lau, J. C. & Linsenmeier, R. A. Oxygen consumption and distribution in the Long-Evans rat retina. *Exp. Eye Res.* **102**, 50–58 (2012).
35. Linsenmeier, R. A. & Braun, R. D. Oxygen distribution and consumption in the cat retina during normoxia and hypoxemia. *J. Gen. Physiol.* **99**, 177–197 (1992).
36. Wilson, D. F. *et al*. Oxygen distribution and vascular injury in the mouse eye measured by phosphorescence-lifetime imaging. *Appl. Opt.* **44**, 5239–5248 (2005).
37. Gray, L. H. & Steadman, J. M. Determination of the oxyhaemoglobin dissociation curves for mouse and rat blood. *J. Physiol* **175**, 161–171 (1964).
38. Dai, C., Liu, X., Zhang, H. F., Puliafito, C. A. & Jiao, S. Absolute retinal blood flow measurement with a dual-beam Doppler optical coherence tomography. *Invest. Ophthalmol. Vis. Sci.* **54**, 7998–8003 (2013).
39. Wehbe, H. *et al*. Automatic retinal blood flow calculation using spectral domain optical coherence tomography. *Opt. Express* **15**, 15193–15206 (2007).
40. Liu, W., Liu, T., Song, W., Yi, J. & Zhang, H. F. Automatic retinal vessel segmentation based on active contours method in Doppler spectral-domain optical coherence tomography. *J. Biomed. Opt.* **18**, 16002 (2013).
41. Choi, W. *et al*. Measurement of pulsatile total blood flow in the human and rat retina with ultrahigh speed spectral/Fourier domain OCT. *Biomed. Opt. Express* **3**, 1047–1061 (2012).
42. Wanek, J., Teng, P. Y., Albers, J., Blair, N. P. & Shahidi, M. Inner retinal metabolic rate of oxygen by oxygen tension and blood flow imaging in rat. *Biomed. Opt. Express* **2**, 2562–2568 (2011).
43. Radhakrishnan, H. & Srinivasan, V. J. Multiparametric optical coherence tomography imaging of the inner retinal hemodynamic response to visual stimulation. *J. Biomed. Opt.* **18**, 86010 (2013).
44. Hammer, M., Leistritz, S., Leistritz, L. & Schweitzer, D. Light paths in retinal vessel oximetry. *Biomedical Engineering, IEEE Transactions on.* **48**, 592–598 (2001).
45. Liu, Y., Zhang, C. & Wang, L. V. Effects of light scattering on optical-resolution photoacoustic microscopy. *J. Biomed. Opt.* **17**, 126014 (2012).
46. Remtulla, S. & Hallett, P. E. A schematic eye for the mouse, and comparisons with the rat. *Vision Res* **25**, 21–31 (1985).
47. Harmening, W. M., Tiruveedhula, P., Roorda, A. & Sincich, L. C. Measurement and correction of transverse chromatic offsets for multi-wavelength retinal microscopy in the living eye. *Biomed. Opt. Express* **3**, 2066–2077 (2012).
48. Song, W. *et al*. Multimodal photoacoustic ophthalmoscopy in mouse. *J. Biophotonics* **6**, 505–512 (2013).
49. Li, H., Dong, B. Q., Zhang, Z., Zhang, H. F. & Sun, C. A transparent broadband ultrasonic detector based on an optical mirco-ring resonator for photoacoustic microscopy. *Sci. Rep.* **4**, 4496; DOI:10.1038/srep04496 (2014).
50. Hammer, M. *et al*. Retinal venous oxygen saturation increases by flicker light stimulation. *Invest. Ophthalmol. Vis. Sci.* **52**, 274–277 (2011).
51. Polak, K., Schmetterer, L. & Riva, C. E. Influence of flicker frequency on flicker-induced changes of retinal vessel diameter. *Invest. Ophthalmol. Vis. Sci.* **43**, 2721–2726 (2002).
52. Leitgeb, R. A., Werkmeister, R. M., Blatter, C. & Schmetterer, L. Doppler Optical Coherence Tomography. *Prog. Retin. Eye Res.* **41**c, 26–43 (2014).
53. Harris, A. L. Hypoxia--a key regulatory factor in tumour growth. *Nat. Rev.Cancer* **2**, 38–47 (2002).
54. Minoshima, S. *et al*. Metabolic reduction in the posterior cingulate cortex in very early Alzheimer's disease. *Ann. Neurol.* **42**, 85–94 (1997).
55. Poehlman, E. T., Scheffers, J., Gottlieb, S. S., Fisher, M. L. & Vaitekevicius, P. Increased resting metabolic rate in patients with congestive heart failure. *Ann. Intern. Med.* **121**, 860–862 (1994).
56. Song, W. *et al*. Integrating photoacoustic ophthalmoscopy with scanning laser ophthalmoscopy, optical coherence tomography, and fluorescein angiography for a multimodal retinal imaging platform. *J. Biomed. Opt.* **17**, 061206 (2012).
57. Radhakrishnan, H. & Srinivasan, V. J. Multiparametric optical coherence tomography imaging of the inner retinal hemodynamic response to visual stimulation. *J. Biomed. Opt.* **18**, 86010 (2013).
58. Zhang, H. F., Maslov, K., Sivaramakrishnan, M., Stoica, G., & Wang, L. V. Imaging of hemoglobin oxygen saturation variations in single vessels in vivo using photoacoustic microscopy. *Appl. Phys. Lett.* **90**, 053901 (2007).
59. Makita, S., Hong, Y., Yamanari, M., Yatagai, T. & Yasuno, Y. Optical coherence angiography. *Opt. Express* **14**, 7821–7840 (2006).
60. Singh, A. S., Kolbitsch, C., Schmoll, T. & Leitgeb, R. A. Stable absolute flow estimation with Doppler OCT based on virtual circumpapillary scans. *Biomed. Opt. Express* **1**, 1047–1058 (2010).

Acknowledgments

This work is supported in part by the NIH grants 1R01EY019951 and 1R24EY022883. It is also supported in part by the NSF grants CBET-1055379, DBI-1353952, and CBET-1066776. W. Song was partially supported by the China Scholarship Council. W. Liu is supported by the Howard Hughes Medical Institute International Student Research Fellowship.

Author contributions

H.F.Z. and S.L.J. initiated the project. H.F.Z. supervised the project. W.S., Q.W., W.Z.L. and T.L. performed the experiments and analyzed the results. W.S., Q.W., W.Z.L., T.L., J.Y., N.S., A.A.F., R.A.L., S.L.J. and H.F.Z. discussed the results and contributed to the manuscript.

Additional information

Supplementary information accompanies this paper at http://www.nature.com/scientificreports

Competing financial interests: The authors declare no competing financial interests.

How to cite this article: Song, W. *et al*. A combined method to quantify the retinal metabolic rate of oxygen using photoacoustic ophthalmoscopy and optical coherence tomography. *Sci. Rep.* **4**, 6525; DOI:10.1038/srep06525 (2014).